Mode water ventilation and subtropical countercurrent over the North Pacific in CMIP5 simulations and future projections

Lixiao Xu,[1,2] Shang-Ping Xie,[1,2] and Qinyu Liu[1]

Received 19 July 2012; revised 16 October 2012; accepted 17 October 2012; published 12 December 2012.

[1] Seventeen coupled general circulation models from the Coupled Model Intercomparison Project Phase 5 (CMIP5) are analyzed to assess the dynamics and variability of the North Pacific Subtropical Countercurrent (STCC). Consistent with observations, the STCC is anchored by mode water to the north. For the present climate, the STCC tends to be stronger in models than in observations because of too strong a low potential vorticity signature of mode water. There are significant variations in mode water simulation among models, i.e., in volume and core layer density. The northeast slanted bands of sea surface height (SSH) anomalies associated with the STCC variability are caused by variability in mode water among models and the Hawaii islands are represented in some models, where the island-induced wind curls drive the Hawaiian Lee Countercurrent (HLCC) located to the south of STCC. Projected future changes in STCC and mode water under the Representative Concentration Pathways (RCP) 4.5 scenario are also investigated. By combining the historical and RCP 4.5 runs, an empirical orthogonal function analysis for SSH over the central subtropical gyre (160°E–140°W, 15°–30°N) is performed. The dominant mode of SSH change in 17 CMIP5 models is characterized by the weakening of the STCC because of the reduced formation of mode water. The weakened mode water is closely related to the increased stratification of the upper ocean, the latter being one of the most robust changes as climate warms. Thus the weakened STCC and mode water are common to CMIP5 future climate projections.

Citation: Xu, L., S.-P. Xie, and Q. Liu (2012), Mode water ventilation and subtropical countercurrent over the North Pacific in CMIP5 simulations and future projections, *J. Geophys. Res.*, *117*, C12009, doi:10.1029/2012JC008377.

1. Introduction

[2] In the central subtropical gyre of the North Pacific (20°–30°N), there is a shallow eastward current named the Subtropical Countercurrent (STCC). It flows against the broad westward flow depicted by the classical Sverdrup theory at these latitudes, and is a robust feature of the subtropical gyre [*Yoshida and Kidokoro*, 1967; *Uda and Hasunuma*, 1969; *White et al.*, 1978; *Kobashi et al.*, 2006]. This surface intensified eastward countercurrent is accompanied by a temperature and density front at subsurface depth of about 100–200 m [*Uda and Hasunuma*, 1969]. According to the hydrographic analysis of *Kobashi et al.* [2006], there are three distinct STCCs, together with three subsurface fronts. The strong STCC front in spring affects surface wind curl, precipitation, and water vapor content with a deep vertical extent, through generations of low-pressure systems of a subsynoptic scale [*Kobashi et al.*, 2008].

[3] With new development of satellite and Argo profiling floats for the past decade, mode water research has advanced greatly [*Oka and Qiu*, 2012]. Mode water, characterized by a minimum in the vertical gradient of temperature and density in the upper thermocline (a thermostad or pycnostad), is not simply a passive water mass. Its distinct low potential vorticity (PV) values suggest potential dynamical effect on ocean circulation [*Xie et al.*, 2012]. Together with theories, recent enhanced observations and model simulations have revealed the importance of mode water in the existence and variability of STCC. Formed in the deep winter mixed layer of the Kuroshio-Oyashio Extension (KOE) east of Japan, the North Pacific subtropical mode water (STMW) [*Suga et al.*, 1989] and central mode water (CMW) [*Nakamura*, 1996; *Suga et al.*, 1997] are advected southeastward riding on the subtropical gyre. Because of the beta spiral effect, mode water of different densities crosses their paths on the horizontal plane as they circulate southward [*Suga et al.*, 2004], and eventually stack up vertically to form a thick low PV

[1]Physical Oceanography Laboratory and Ocean-Atmosphere Interaction and Climate Laboratory, Ocean University of China, Qingdao, China.
[2]International Pacific Research Center and Department of Meteorology, University of Hawai‘i at Mānoa, Honolulu, Hawaii, USA.

Corresponding author: L. Xu, Physical Oceanography Laboratory, Ocean University of China, 238 Songling Rd., Qingdao 266100, China. (xulixiao2004@126.com)

0148-0227/12/2012JC008377

Table 1. List of 17 Models From CMIP5 Analyzed in This Study

Model	Institution
CNRM-CM5	Centre National de Recherches Meteorologiques (France)
GFDL-ESM2M	NOAA/Geophysical Fluid Dynamics Laboratory
HadGEM2-CC	Met Office Hadley Centre
bcc-csm1-1	Beijing Climate Center, China Meteorological Administration
MRI-CGCM3	Meteorological Research Institute, Tsukuba, Japan
CanESM2	Canadian Centre for Climate Modeling and Analysis
IPSL-CM5A-LR	Institute Pierre-Simon Laplace, Paris, France
HadGEM2-ES	Met Office Hadley Centre
MIROC5	University of Tokyo, NIES, and JAMSTEC
MPI-ESM-LR	Max Planck Institute for Meteorology
IPSL-CM5A-MR	Institute Pierre-Simon Laplace, Paris, France
MIROC-ESM	University of Tokyo, NIES, and JAMSTEC
MIROC-ESM-CHEM	University of Tokyo, NIES, and JAMSTEC
FGOALS-g2	Institute of Atmospheric Physics, Chinese Academy of Sciences
FGOALS-s2	Institute of Atmospheric Physics, Chinese Academy of Sciences
GISS-E2-R	NASA Goddard Institute for Space Studies, New York, NY
NorESM1-M	Norwegian Climate Centre

pool [*Kubokawa*, 1999]. This thick low PV pool pushes the upper thermocline to shoal, leading to an eastward countercurrent on the southern flank, as illustrated by *Kubokawa and Inui* [1999] in an idealized ocean general circulation model. Together with *Aoki et al.* [2002], the hydrographic analysis of *Kobashi et al.* [2006] confirmed that the STCC is anchored by mode water beneath to the south. The slanted STCC stretching from the western Pacific to the north of Hawaii, just to the south of the mode water, is itself suggestive of the mode water's dynamical effect on STCC.

[4] Mode water–induced variations in ocean current are dominant on timescales longer than interannual [*Nonaka et al.*, 2012]. Such changes in mode water induce variations of STCC on longer timescales. In an eddy resolving ocean general circulation model (OGCM), *Yamanaka et al.* [2008] show that the STCC intensifies in the late 1970s with a strong southward intrusion of mode water and weakens in the early 1990s when mode water ventilation is weak. Using a 300 year control simulation from the Geophysical Fluid Dynamics Laboratory (GFDL) coupled model CM2.1, *Xie et al.* [2011] show that on decadal time scales, the dominant mode of sea surface height (SSH) variability in the central subtropical gyre (170°E–130°W, 15°–35°N) is characterized by the strengthening and weakening of the STCC as a result of variations in mode water ventilation. This STCC mode of natural variability is excited by global warming, resulting in banded structures in sea surface warming that slant in a northeast direction, with a striking similarity with the negative phase of the decadal STCC mode [*Xie et al.*, 2011; *Xu et al.*, 2012]. In the global warming simulation, less mode water is produced on lighter isopycnal surfaces, decelerating the STCC and leaving banded structures on SSH and sea surface temperature (SST).

[5] These results are based on one single coupled model, and their validity needs to be examined in more models. Until longer and denser observations become available, general circulation models (GCMs) will remain the main tool to study slow variability of STCC and mode water. Assessing model's performance in representing the STCC and mode water is the first step toward improving simulating these phenomena and predicting their change under global warming.

[6] The present study assesses 17 CGCMs from the Coupled Model Intercomparison Project Phase 5 (CMIP5), focusing on the dynamical effect of mode water ventilation on STCC. It represents the first multimodel study on the dynamics and variability of the STCC. We wish to address the following questions: Can the CMIP5 models simulate the STCC, and what role does mode water play? What are the common features and major differences related to mode water and STCC among models? How do the CMIP5 simulations compare with observations? How will the STCC and mode water respond to global warming? We will show that the STCC is anchored by mode water, much as in observations. Intermodel variability of mode water causes significant STCC changes among models. The mode water consistently weakens in global warming, and so does the STCC in all the 17 CMIP5 models evaluated here.

[7] The rest of the paper is organized as follows. Section 2 briefly describes the data source and analysis method. Section 3 evaluates the present-day climatology including both the ensemble mean and the intermodel diversity with regard to STCC dynamics, and compares with observations where appropriate. Section 4 investigates the simulated response of STCC and mode water to global warming. Section 5 is a summary.

2. Data and Method

[8] We used the following observational data sets for comparison with models: the mean SSH field from MDT_CNES-CLS09 [*Rio et al.*, 2011], which combines the GRACE geoid, surface drifter velocities, profiling floats, and hydrographic temperature–salinity data; the 1° × 1° gridded monthly climatology of Argo data including MLD, potential temperature, salinity and potential density from International Pacific Research Center (IPRC), linearly interpolated to 26 standard levels from 0 to 2000 m; and the wind stress climatology from Quick Scatterometer (QuikSCAT).

[9] The model output used in this study is from seventeen coupled climate models (Table 1) as part of the CMIP5, which offers a multimodel perspective of simulated climate variability and change [*Taylor et al.*, 2012]. Both the historical (20th century with all forcing simulation) and the Representative Concentration Pathways (RCP) 4.5 scenario (approximately with a radiative forcing of 4.5 W m^{-2} at year 2100, relative to preindustrial conditions) are used. The model output is freely available from the Program for Climate Model Diagnosis and Intercomparison (PCMDI) at the Lawrence Livermore National Laboratory (http://cmip-pcmdi.llnl.gov/cmip5/).

[10] The spatial resolution varies between models and within the same model for atmospheric and oceanic variables. To facilitate comparison with each other and observations, we interpolated them onto a 1°×1° latitude-longitude grid. We investigate both the common features (ensemble mean) and the intermodel difference among models, focusing on the STCC dynamics and variability. The present-day climatology is based on the time average

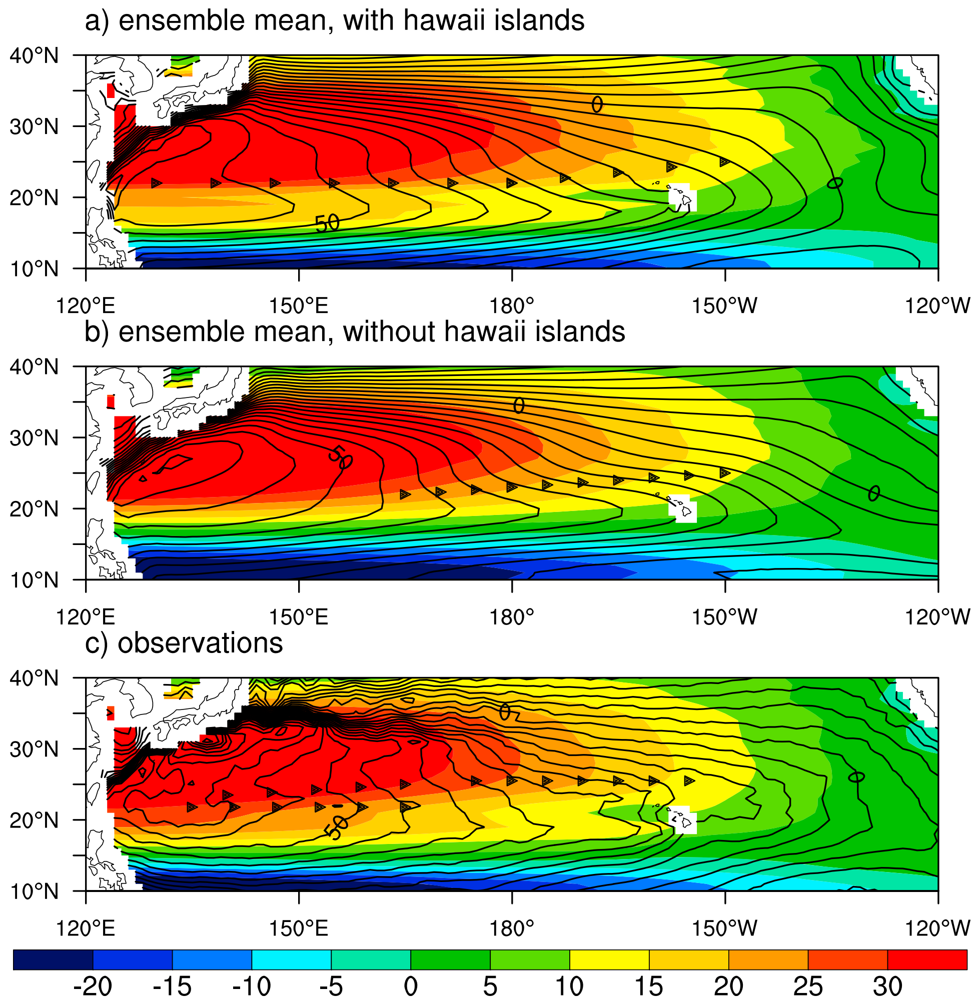

Figure 1. Present-day climatology (1951–2000) of Sverdrup stream function (color shaded in *Sv* (10^6 m^3 s^{-1})) and SSH (black contours in 5 cm intervals): ensemble mean of models that (a) present and (b) do not represent Hawaii islands and (c) observations. The position of STCC is marked out by triangles.

from 1951 to 2000 in historical run, while the future mean state is taken from 2051 to 2100 in RCP 4.5. The present-day climatology calculated for different periods (e.g., 10, 20, or 50 years) is mutually similar in CMIP5 models (not shown here). So we use the 50 year based present-day climatology to compare with observations. For each model only one member run is analyzed (usually "rli1p1"). (r < N > i < M > p < L>) denotes member run for a single model. This triad of integers (N, M, L), formatted as shown above (e.g., "r1i1p1") distinguishes among closely related member runs by the same model. N, M and L are associated with a specific initial condition, initialization method, and perturbed physics version, respectively.

[11] An ensemble-mean statistic is the average of all models. As an example, the Sverdrup stream function is first computed for each model, and then is averaged for 17 models (Figure 1). The ensemble mean PV in Figures 3 and 4 is averaged on isopycnals.

3. STCC and Mode Water in Present Climate

[12] This section examines the reproducibility of STCC and mode water in CMIP5 models for present-day climate. We first examine the simulations of STCC, then discuss its relationship to mode water, and finally show the intermodel variability.

3.1. STCC Distribution

[13] This section examines the STCC distribution from the SSH field. Figure 1 compares the annual mean SSH field and Sverdrup stream function for the ensemble mean and observations. We separate the ensemble mean into two groups: 6 models (CNRM-CM5, HadGEM2-CC, CanESM2, HadGEM2-ES, MIROC5, GISS-E2-R) that include the Hawaii islands (Figure 1a), and those that do not (Figure 1b) (11 models: GFDL-ESM2M, bcc-csm1-1, MRI-CGCM3, IPSL-CM5A-LR, MPI-ESM-LR, IPSL-CM5A-MR, MIROC-ESM, MIROC-ESM-CHEM, FGOALS-g2, FGOALS-s2, NorESM1-M). The main difference between Figures 1a and 1b is the Hawaii Lee countercurrent (HLCC). The HLCC is an eastward current located west of the Hawaii islands, driven by island-induced wind curls [*Xie et al.*, 2001; *Sakamoto et al.*, 2004]. Consistent with the Sverdrup flow, HLCC is present in models where the Hawaii islands are represented (Figure 1a). Compared to CMIP3, the HLCC is one of the new improvements in CMIP5 because of increased resolution.

[14] The models simulate a basin scale anticyclonic subtropical gyre circulation. Marked as triangles in Figure 1, the STCC is embedded in the central gyre (20°–30°N) where the SSH contours in CMIP5 ensembles veer northwestward (Figures 1a and 1b). The current deviates strongly from and flows against the Sverdrup flow. The comparison of Figures 1a and 1b indicates the difference between HLCC and STCC. For observations, Figure 1c shows two distinct SSH ridge in the central subtropical gyre. The northern branch against the Sverdrup stream function is STCC, while the southern branch consistent with the Sverdrup flow is HLCC. For CMIP5 models, there is no distinct separation in SSH ridge between STCC and HLCC (Figure 1a). According to the hydrographic study of *Kobashi et al.* [2006], there are three distinct STCCs in observations: the northern and southern currents in the western basin, and the eastern STCC in the central basin (Figure 1c), structures that the models do not capture. In the CMIP5 models, the band of the eastern STCC apparently continues from the southern STCC. The position of STCC in CMIP5 models is more southerly (1 $\sim$ 2° latitudes) than observations, and the averaged velocity of STCC is stronger: $\sim$4 cm/s in CMIP5 models and $\sim$2 cm/s in observations. It is closely related to too strong mode water to the north, as will be discussed next. Note that no further distinction is made between models with and without the Hawaii Islands after this section.

3.2. Relationship Between STCC and Mode Water

[15] This section relates the mode water ventilation to STCC. We first give the physical basis, and then test its validity in CMIP5 models. The physical analysis procedure is based on *Kobashi et al.* [2006], here we introduce a new, accumulative variable "bulk thickness," to highlight the accumulated effect of low PV waters on STCC formation.

3.2.1. Physical Basis

[16] Under the assumption of negligible relative vorticity, PV q is given on a vertical coordinate of density ρ by

$$q(\rho) = -\frac{f}{\rho_0}\left(\frac{\partial z}{\partial \rho}\right)^{-1}, \tag{1}$$

where z is the depth of isopycnal surface (negative under the sea surface), f is the planetary vorticity, and ρ_o is the reference density taken as the lower boundary of the low PV layer. The minus sign is introduced because $\frac{\partial z}{\partial \rho}$ is negative for a stable stratified ocean. Solving for z leads to

$$z(\rho) = -\frac{1}{\rho_0}\int_{\rho_b}^{\rho}\left(\frac{f}{q(\rho')}\right)d\rho' + z_0(\rho_b), \tag{2}$$

where z_0 is the depth of a reference isopycnal surface $\rho_b(\geq\rho)$. If we defined the bulk thickness of the low PV layer (bulk thickness in short hereafter) as

$$Q = -\frac{1}{\rho_0}\int_{\rho_b}^{\rho_a}\left(\frac{f}{q(\rho')}\right)d\rho' = z(\rho_a) - z_0(\rho_b), \tag{3}$$

where ρ_a is a density lighter than the mode water, the bulk thickness Q represents the thickness of a layer that contains the mode water. The equation (2) becomes

$$z(\rho_a) = Q + z_0(\rho_b). \tag{4}$$

Taking the meridional derivative yields

$$\left(\frac{\partial z(\rho_a)}{\partial y}\right)_\rho = \frac{\partial Q}{\partial y} + \left(\frac{\partial z_0(\rho_b)}{\partial y}\right)_\rho, \tag{5}$$

where the subscript ρ denotes that the partial derivative is taken on a constant ρ surface.

[17] The left hand side of equation (5) is the slope of the isopycnal surface above the mode water layer, and the right hand side is the deviation of meridional bulk thickness gradient. Thus, equation (5) states that the meridional slope of an upper isopycnal (related to zonal current shear by thermal wind) is related to the bulk thickness gradient. If we choose the lower pycnocline as a deep isopycnal ρ_b in equation (5), the slope $\left(\frac{\partial z_0(\rho_b)}{\partial y}\right)_\rho$ is negative in the central North Pacific. In order for $\left(\frac{\partial z(\rho_a)}{\partial y}\right)_\rho$ to be positive (for an eastward flowing STCC), the bulk thickness gradient $\frac{\partial Q}{\partial y}$ must take a large positive value. This means a large bulk thickness must be located to the north of the eastward countercurrent.

3.2.2. Bulk Thickness and STCC

[18] The core layer density of mode water varies considerably among models, and it is difficult to evaluate mode water volume for multimodel comparison and ensemble mean. Bulk thickness overcomes this shortcoming and is convenient for the multimodel study. Instead of calculating PV on individual isopycnal surfaces, the present study directly relates the bulk thickness to the STCC formation. After investigating the climatological thermocline structure in the central North Pacific, we choose to calculate the bulk thickness as the difference of isopycnal depth between the seasonal (24.5 σ_θ) and permanent (26.6 σ_θ; largely unventilated) thermocline because this layer contains the mode water. As in observations, there is a large bulk thickness value located in the central subtropical gyre just to the north of the STCC (Figure 2). The STCC is anchored by this large positive bulk thickness gradient on the southern edge of the band of large Q, consistent with equation (5). This thick low PV layer causes the upper pycnocline to rise, forming a density front and a surface intensified eastward countercurrent to the south.

3.2.3. Mixed Layer Depth and Bulk Thickness

[19] The mixed layer depth (MLD), defined as the depth at which the water density is 0.03 kg m^{-3} denser than the sea surface, reaches its seasonal maximum in March for the North Pacific. The simulated MLD is deepest ($\sim$200 m) in KOE east of Japan (Figure 3a). Separating this deep mixed layer region from the rest of the North Pacific is a narrow transition zone called the MLD front, key to the formation of low PV waters [*Kubokawa*, 1997, 1999]. The low PV water north of STCC is subducted from the intersections of outcrop lines and MLD front [*Xie et al.*, 2000]. The MLD front slants slightly northeastward from the western subtropical gyre, while outcrop lines are almost zonal and slant slightly southeastward. As the outcrop line of increasing density intersects the MLD front successively northeastward, the low PV fluids on denser isopycnals are formed in the northeast [*Kobashi and Kubokawa*, 2012]. As in observations [*Kobashi et al.*, 2006] and Kubokawa's theory,

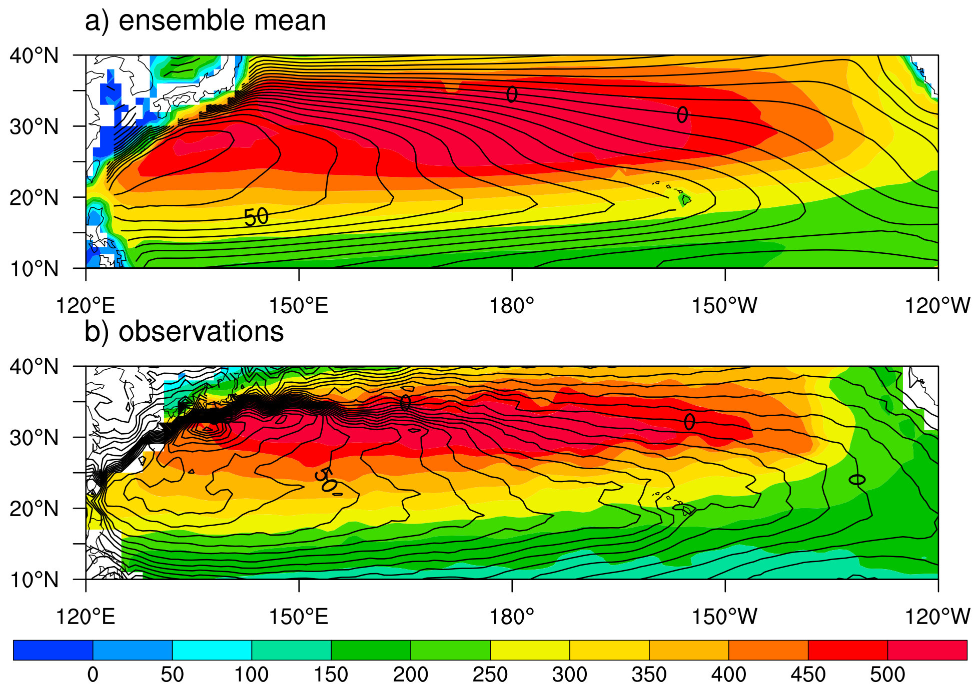

Figure 2. Present-day climatology (1951–2000) of SSH (black contours in 5 cm intervals) and bulk thickness of the layer between 24.5 σ_θ and 26.6 σ_θ (color shade in 50 m intervals) for (a) ensemble mean and (b) observations.

trajectories of these minimum PV fluids on isopycnals converge on the horizontal plane as they are advected southward, and the low PV fluids are stacked up vertically and form a thick layer of low PV fluids. The subduction rate and thus the volume of low PV waters are proportional to the strength of the MLD front [*Xie et al.*, 2000]. Thus the bulk thickness of the low PV layer is closely related to the MLD front strength.

[20] In observations, MLD maxima (>150 m) are organized in two zonal bands along 32°N and 42°N (Figure 3b). The northern band of the deep MLD extending to 160°W is associated with CMW, and the southern band extending to 170°E is associated with STMW. CMIP5 models do not capture this feature, with one single pool of deep MLD and a sharp MLD front that slants northeastward (Figure 3a). The low PV tongue on core layers of STMW and CMW is much weaker in observations than in CMIP5 models. The area of PV lower than 2.0×10^{-10}m^{-1} s^{-1} in observations is limited to near the formation region and dissipated quickly southward (Figure 3b), while the low PV area in CMIP5 models extends much farther to southwestward (Figure 3a). Because of the excessively strong MLD front and low PV tongues in Figure 3a, the bulk thickness (especially the eastern part related to the CMW) seems to be overestimated in CMIP5 models (Figure 2).

3.3. Intermodel Difference

[21] This section analyzes intermodel variability in STCC and mode water simulations among 17 CMIP5 models. We first compare the STMW and CMW simulation in different models, and then relate this intermodel diversity of mode water to the STCC variability among models.

3.3.1. Distribution of Mode Water

[22] Figure 4 shows the total volume of low PV cores over the North Pacific (120°E–140°W; 20°–40°N) as a function of density in 17 CMIP5 models and observations. The low PV core is defined as the vertical PV minimum (<1.5×10^{-10}m^{-1}s^{-1}) in the density range of 24.0 ~ 27.0 σ_θ, which includes STMW and CMW for both CMIP5 models and observations (not shown). Following *Kobashi et al.* [2006], the volume of the PV cores is taken as the thickness between isopycnals of its core layer density ±0.05 kg m^{-3}.

[23] The last two panels of Figure 4 compare the ensemble mean and Argo results. For Argo observations, the PV minimum appears in two distinct density modes: 24.9−25.4 σ_θ and 25.8–26.1 σ_θ, corresponding to the STMW and CMW, respectively. For the CMIP5 ensemble, low PV water also tends to occur in two modes in denser ranges of 25.5−26.0 σ_θ and 26.1–26.5 σ_θ. The volume of low PV water (especially CMW) is much larger in the CMIP5 ensemble mean than observations because of the sharp MLD front (Figure 3) and the weak dissipation of low PV water in CMIP5. By contrast, in observations the MLD front is weaker, the low PV tongues are much more diffused by eddies [*Oka and Qiu*, 2012], and the CMW formation is not primarily associated with the mixed layer front but due to the cross-isopycnal flow in the mixed layer [*Suga et al.*, 2004]. The core densities of STMW and CMW are ~0.4 denser than in observations.

[24] Mode water properties vary greatly among CMIP5 models in core layer density and the total volume. We rank mode water volume and order panels of Figure 4 from high to low for 17 CMIP5 models. Mode water volume exceeds observations in eleven models (bcc-csm1-1, GFDL-ESM2M, MIROC-ESM-CHEM, MIROC-ESM, MRI-CGCM3, IPSL-

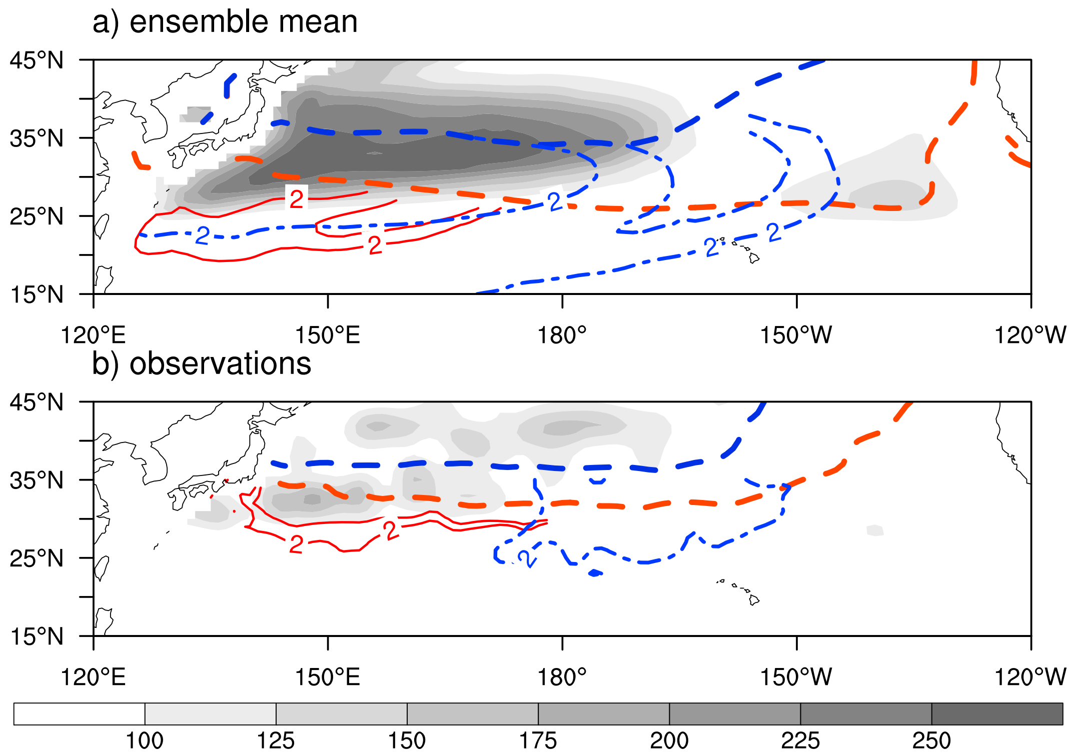

Figure 3. March climatology (1951–2000). (a) CMIP5 ensemble mean: PV on 25.8 (red solid contours at 1.5 and 2.0 × $10^{-10}m^{-1}$ s^{-1}) and 26.3 (blue dash-dotted contours) isopycnals, along with the mixed layer depth (gray shade >100 m) and surface density (dashed contours, red for 25.8 σ_θ and blue for 26.3 σ_θ). (b) Observations: PV on 25.2 (red solid contours at 1.5 and 2.0 × $10^{-10}m^{-1}$ s^{-1}) and 26.0 (blue dash-dotted contours) isopycnals, along with the mixed layer depth (gray shade >100 m) and surface density (dashed contours, red contour for 25.2 σ_θ and blue for 26.0 σ_θ). The lighter low PV layer (red solid contours) is corresponding to the core layer of STMW, while the denser layer (blue dash-dotted contours) corresponds to the core layer of CMW.

CM5A-LR, GISS-E2-R, IPSL-CM5A-MR, FGOALS-g2, MIROC5, MIPI-ESM-LR). Three models (CanESM2, FGOALS-s2, NorESM1-M) show a too small mode water volume.

3.3.2. Dynamical Effect of Mode Water on STCC

[25] Based on mode water volume, we composite the SSH anomalies (models with high mode water volume minus those with low mode water volume). Figure 5 shows the SSH difference between models with high (bcc-csm1-1, GFDL-ESM2M, MIROC-ESM-CHEM, MIROC-ESM, MRI-CGCM3, IPSL-CM5A-LR, GISS-E2-R, IPSL-CM5A-MR, FGOALS-g2) and low (MIROC5, MIPI-ESM-LR, CNRM-CM5, HadGEM2-CC, HadGEM2-ES, CanESM2, FGOALS-s2, NorESM1-M) mode water volumes. The SSH anomalies in Figure 5 feature the northeast slanted dipole pattern that strengthens the STCC. Thus models with stronger (weaker) mode water show a stronger (weaker) STCC. The scatterplot of Figure 6 also supports the close relationship between STCC and mode water volume. The coupled variability between STCC and mode water among models gives further support for the mode water's dynamical effect on STCC.

[26] In summary, the CMIP5 models capture the mode water's dynamical effect on STCC for the present climate. Mode water forces the seasonal thermocline to shoal, and anchors the surface intensified STCC to the south in the central North Pacific. Compared to observations, the ensemble mean STCC (especially the eastern part) seems to be too strong because of the too strong mode water ventilation. There are significant variations in mode water and STCC simulation among models. Characterized by the northeast slanted bands of SSH anomalies, the STCC variability among models is caused by their difference in mode water volume, illustrating mode water's dynamical role on STCC.

4. Response to Global Warming

[27] This section investigates how the STCC and mode water evolve with global warming in CMIP5 models. We first show the STCC change, and then relate it to mode water change. Both the ensemble mean of the mean state change and the time evolution in individual models are investigated.

4.1. STCC Response

[28] Figure 7 shows the ensemble mean SSH difference from (1951~2000) to (2051~2100), superimposed on the present-day climatology of SSH (1951–2000). As climate warms, SSH increases in the whole basin. A band of minimum in SSH increase is collocated with the mean SSH ridge where STCC is located. The banded structure of SSH anomalies represents a weakening of STCC, similar as our

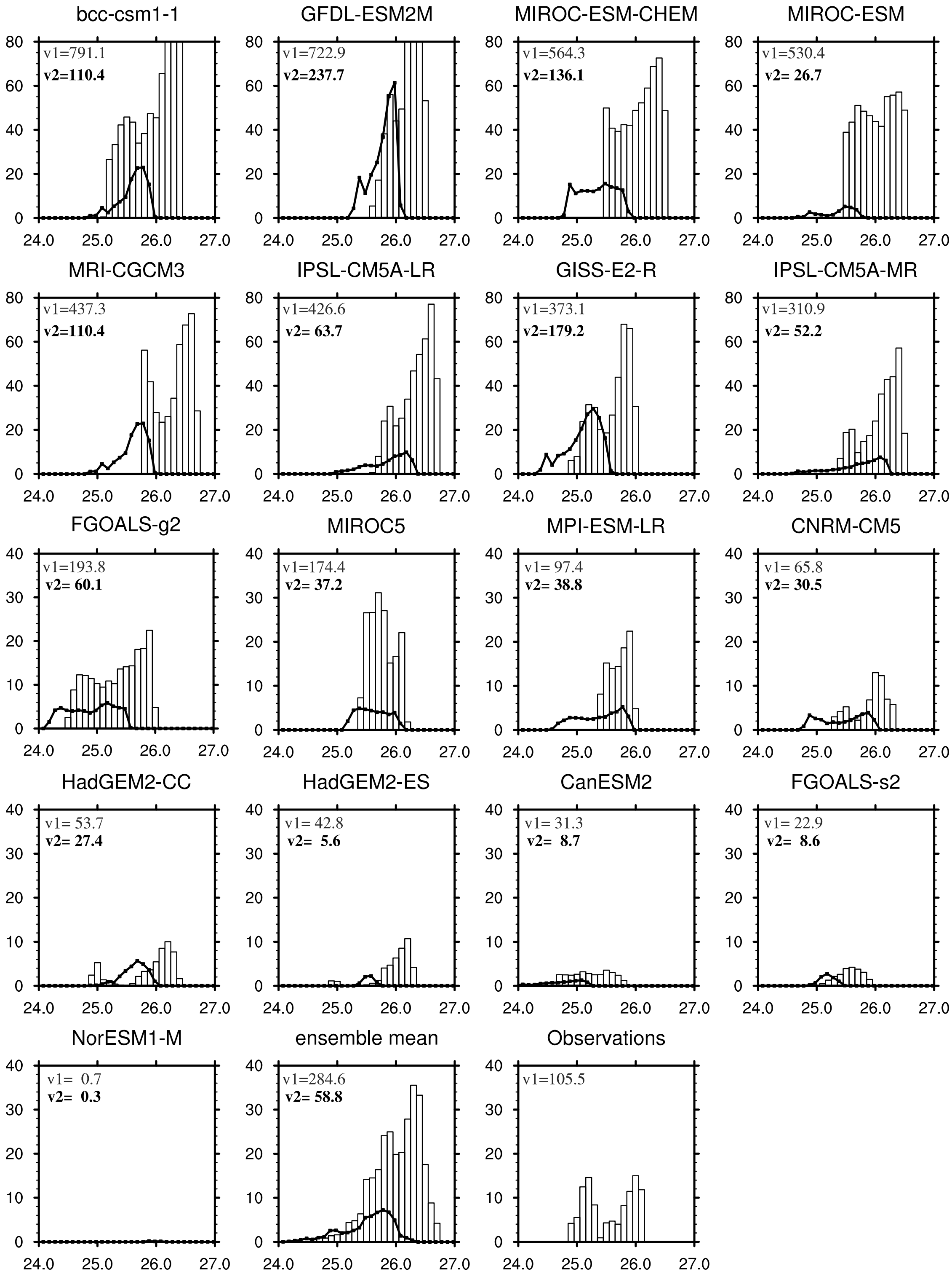

Figure 4. Volume (10^{12} m^3) of the minimum PV layer over the North Pacific (120°E–140°W, 20°–40°N) for each density class in present-day climatology (gray bars) and future projections (black lines) in 17 CMIP5 models, ranked from high to low in order of present-day total volume. The total volume for the entire density range in present-day climatology (v1) and future projections (v2) is shown in the top left corner. The last two panels are for the ensemble mean and observations. Note different vertical scales for the first two rows. Vertical extent of the minimum PV layer expands from (rm−0.05) to (rm + 0.05), and rm is the density of the low PV core.

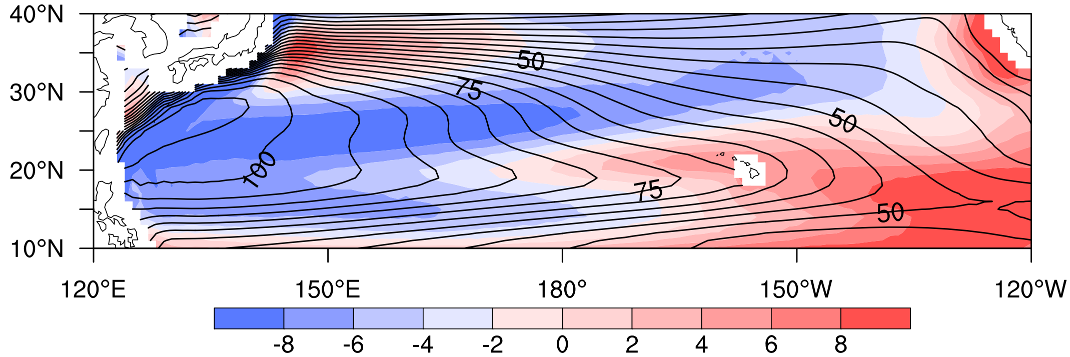

Figure 5. SSH difference between models with high (bcc-csm1-1, GFDL-ESM2M, MIROC-ESM-CHEM, MIROC-ESM, MRI-CGCM3, IPSL-CM5A-LR, GISS-E2-R, IPSL-CM5A-MR, FGOALS-g2) and low (MIROC5, MIPI-ESM-LR, CNRM-CM5, HadGEM2-CC, HadGEM2-ES, CanESM2, FGOALS-s2, NorESM1-M) mode water volumes (color shade in centimeters), superimposed on the present-day ensemble mean climatology of SSH (contours at 5 cm intervals). Note the SSH difference is obtained from models with high mode water minus those with low mode water volume.

previous results from GFDL CM2.1 [*Xie et al.*, 2010, 2011; *Xu et al.*, 2012].

[29] We combine the historical and the RCP 4.5 runs to form a 200 year long data set, and then perform an empirical orthogonal function (EOF) analysis for SSH anomaly in 17 CMIP5 models from 1901 to 2100 in the central subtropical gyre domain (160°E–140°W, 15°–30°N) where the STCC is located. We apply a 9 year low-pass filter to remove high-frequency variability, focusing on the slow STCC and mode water evolution. The spatial pattern (Figure 8) and principal component (PC) (Figure 9a) of the leading mode in 17 CMIP5 models are consistently characterized by the weakening STCC with global warming. The spatial pattern in the ensemble mean features a northeast slanted dipole, with the SSH anomalies in the STCC band roughly in phase with the mean SSH pattern, representing a strengthening of the STCC at the positive phase [*Xie et al.*, 2011; *Xu et al.*, 2012]. A similar dipole pattern is also shown in most of the individual models (especially models with stronger mode waters, i.e., bcc-csm1-1, GFDL-ESM2M, MIROC-ESM-CHEM, MIROC-ESM, MRI-CGCM3, IPSL-CM5A-LR, GISS-E2-R, IPSL-CM5A-MR, FGOALS-g2, MIROC5, MPI-ESM-LR, CNRM-CM5, HadGEM2-ES), although the position and strength of the SSH anomalies in relation to the STCC band (Figure 8) vary among models. Corresponding to the spatial SSH dipole patterns, the PC time series in all the CMIP5 models show a consistent decreasing trend in global warming (Figure 9a), illustrating the weakening of STCC from the 21st century.

4.2. Mode Water Change

[30] We investigate the vertical structure of STCC and mode water in warmer climate. Figure 10 compares the ensemble-mean latitude-depth section of zonal velocity and potential density at the international dateline between the present-day climatology and future projections. For the present-day climatology, the STCC is a surface-intensified eastward current confined to the upper 100 m, in thermal wind balance with the northward shoaling of the upper pycnocline ($\sigma_\theta < 25.5$ at this longitude). In 20°–25°N where the STCC is found, the lower pycnocline deepens northward as predicted by the Sverdrup theory. The 25.75 σ_θ isopycnal begins to shoal northward with a thick layer of low PV water found underneath. The 25.5 σ_θ isopycnal shows an ever steeper northward shoaling, pushed by low PV water in the 25.5–26.0 σ_θ layer. For future projections, this overall vertical structure of STCC and its relationship to mode water do not change, indicating that the STCC is still tied to mode waters in RCP 4.5. The upper ocean has a lighter density field (by $\sim$0.5 kg m^{-3}), and is more stratified over the entire depth, similar to the result of our previous studies based on GFDL CM2.1 [*Xu et al.*, 2012]. As mode waters move to lighter isopycnal surfaces, the base of the upper pycnocline that shoals northward changes to 25.25 σ_θ from 25.75 σ_θ in present-day climatology. In addition, the northward shoaling is gentler because of the shrinking mode waters underneath. Consequently, compared to the present-day climatology, the ensemble mean zonal velocity of STCC reduces from 4 cm/s

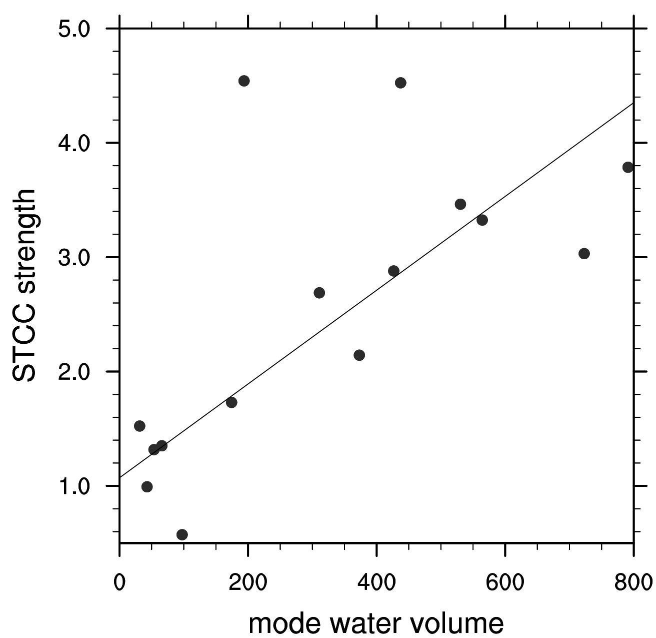

Figure 6. Scatterplot of mode water volume (10^{12} m^3) and STCC strength (cm/s) for 17 CMIP5 models.

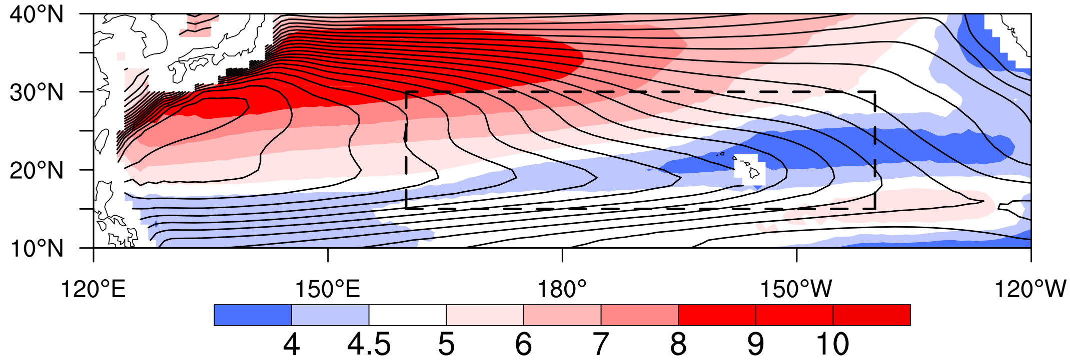

Figure 7. RCP 4.5 (2051–2100) minus historical run (1951–2000) SSH changes (color shade in centimeters), superimposed on ensemble mean SSH for present-day climatology (contours in 5 cm). The box denotes the central gyre domain for the EOF analysis in Figure 8.

to 1 cm/s, and the corresponding eastward STCC depth also shoals from 100 m to 50 m.

[31] Figure 9b shows the time series of the area averaged bulk thickness between $24.5\sigma_\theta$ and $26.6\ \sigma_\theta$ in 120°E∼140°W, 20°∼40°N north of the STCC in 17 CMIP5 models. The bulk thickness shows a consistent decreasing trend in 17 CMIP5 models as the globe warms, in agreement with the weakening STCC in Figure 9a. The bulk thickness in the twentieth century shows a significant decadal variability at a typical time scale of 50 years, but the variability weakens sharply as the

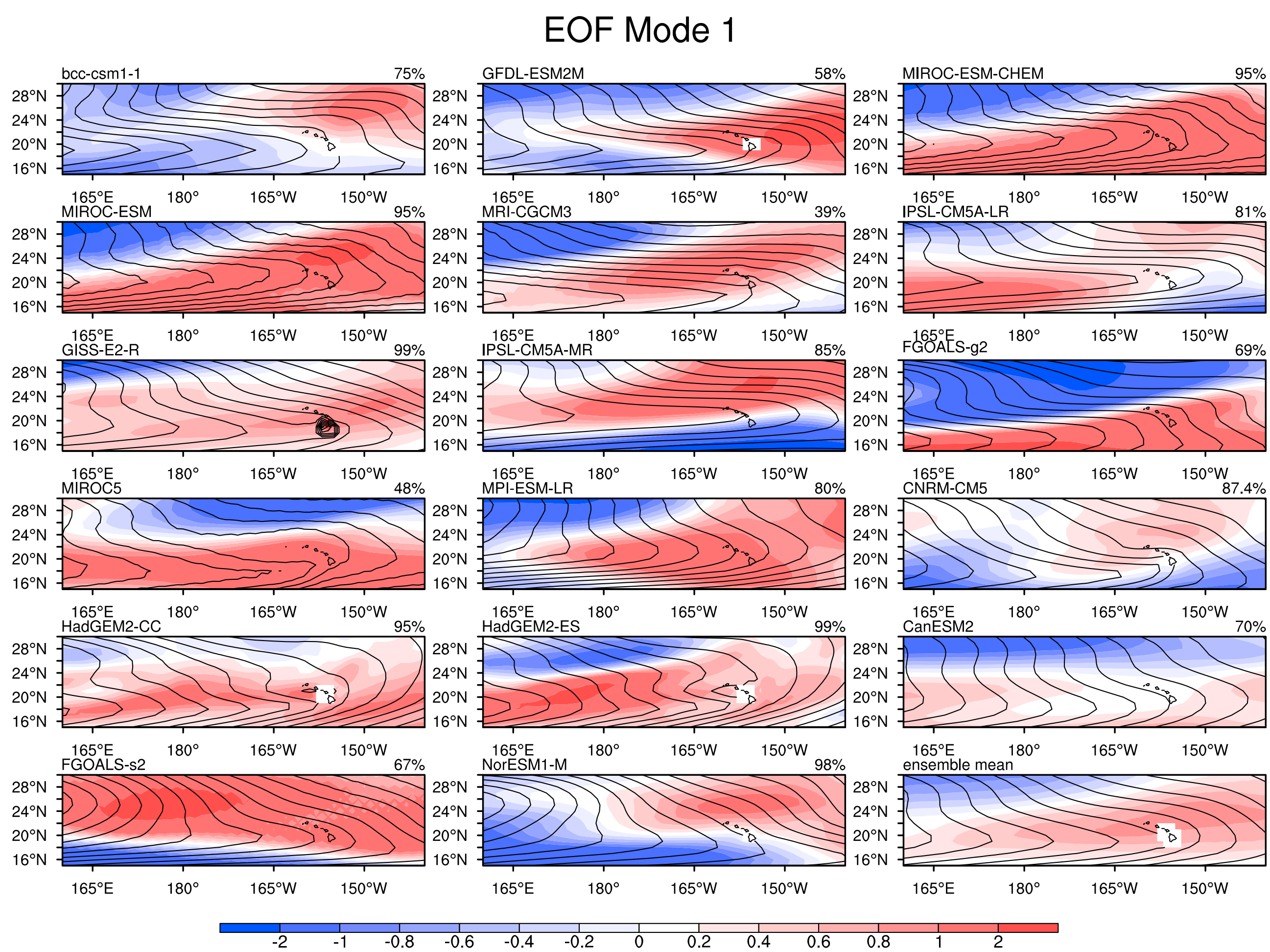

Figure 8. First EOF mode for SSH (color shade in centimeters) in the central subtropical gyre (160°E–140°W, 15°–30°N) for each of the CMIP5 models and the ensemble mean along with the historical mean SSH (black contours in 5 cm) for individual models. The variance fraction explained by the EOF mode is denoted at the top right corner.

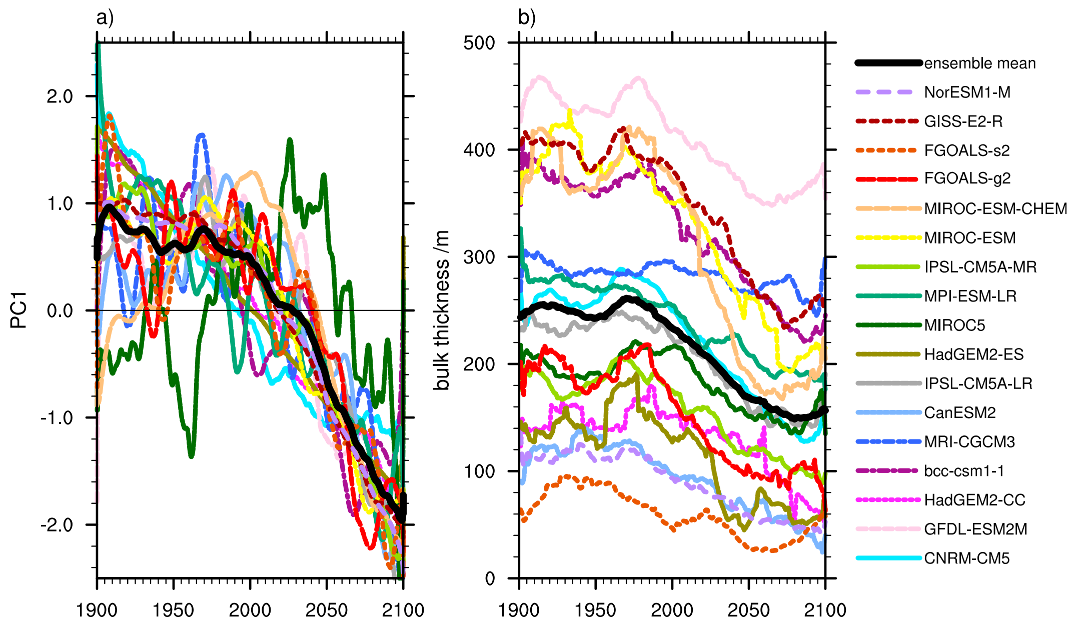

Figure 9. (a) PC of the first EOF mode for SSH in the central subtropical gyre and (b) the averaged bulk thickness between 24.5σ_θ and 26.6 σ_θ over the North Pacific (120°E–140°W, 20°–40°N) in 17 CMIP5 models and ensemble mean as illustrated in the right legend. A 9 year low-pass filter is applied to remove the high-variance variability.

atmospheric CO_2 concentrations increase from 2001 to 2100, though the mean bulk thickness is different among models, the decreasing trend is consistent among models (Figure 9b). The decadal variability in the twentieth century seems to be associated with the model's Pacific Decadal Oscillation (PDO), with the latter affecting MLD in the KOE region and thus the subduction rate [*Qu and Chen*, 2009]. As for the change in density distribution of mode water (black line for after global warming in Figure 4), we find that both peaks in low PV occurrence are markedly diminished and each moves to a lighter density, similar to results of *Luo et al.* [2009b] based on CMIP3 models, and *Xu et al.* [2012] based on GFDL CM2.1. Thus the weakening of mode water is a robust change of global warming.

[32] As climate warms, the ocean warming is greatest near the surface and decreases with depth. The ocean is more stratified and the MLD shoals as a result [*Luo et al.*, 2009a]. The more stratified upper ocean is due mainly to changes in surface heat flux and large-scale wind stress in the warmer climate (Figure 11b). As climate warms, the ocean to atmosphere heat loss is reduced over most of the North Pacific (except for a narrow band around 40°N) especially in the northwest part of the subtropical gyre. Such a change in the heat flux contributes to a more stratified upper ocean and

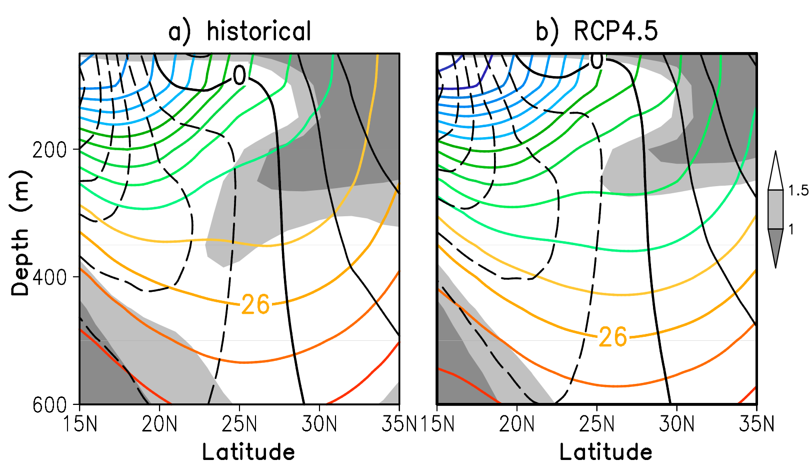

Figure 10. Ensemble-mean March potential density (color contours at 0.25 σ_θ intervals) and zonal velocity (black contours at 0.02 m/s intervals) at 180°E as a function of latitude and depth, along with PV < 1.5 $\times$ $10^{-10}m^{-1}s^{-1}$ in gray shading in (a) present-day (1951–2000) and (b) RCP 4.5 (2051–2100) climatology. The lower thermocline water shaded in the sections is not mode water but represents weak stratification below the thermocline.

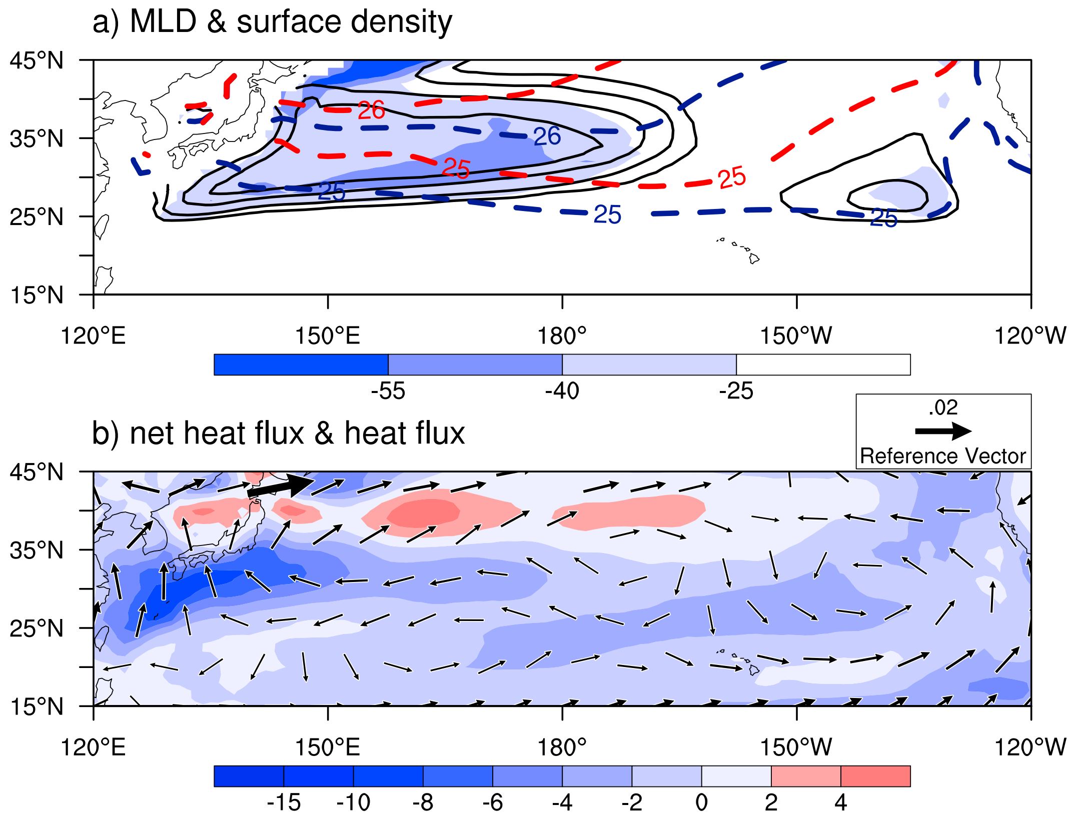

Figure 11. (a) March mean MLD for present-day climatology (>100 m; black contours at 50 m intervals), surface potential density for present-day climatology (blue dashed contours) and for future projections (red contours), superimposed with MLD change in global warming (RCP 4.5 (2051–2100) minus historical run (1951–2000)) (<–25 m in color shade). (b) Differences of wind stress (*Pa*) and ocean-to-atmosphere heat flux (color in W m^{-2}).

resultant shoaling of the MLD. In terms of changes in the large-scale wind stress, the weakened westerlies over the KE can contribute to the surface warming, and a more stratified upper ocean conditions unfavorable for the mode water formation. The maximum shoaling of MLD (<–40 m) takes place on the southern flank of the deep MLD between 150°E and the dateline along about 30°N, weakening the MLD front to the south (Figure 11a). As a result, the mode water subduction is reduced and takes place on lighter isopycnal surfaces, as surface density decreases and outcrop lines move northward. The more stratified upper ocean is one of the most robust changes in global warming. We show that the resultant weakening of the mode water and STCC is equally robust across models; the shoaling mixed layer and resultant reduction in mode water subduction contribute to the enhancement of subtropical upper ocean stratification.

5. Summary

[33] We have examined the dynamical effect of mode water ventilation on STCC in 17 CMIP5 models. As in observations, the STCC is anchored by mode water to the north. We define a bulk thickness to represent the vertical accumulation of low PV waters. The STCC formation is directly related to the meridional PV gradient of the bulk mode water layer thickness instead of low PV on individual isopycnal surfaces. Compared to observations, the bulk thickness in CMIP5 ensemble mean is too large, resulting in a too strong STCC. The overestimated mode water is caused by both a strong MLD front and the weak dissipation on low PV waters, deficiencies common to climate models. Furthermore, the mode water volume and its core layer density vary from models. The intermodel variability of mode water causes the STCC variability in intensity and position among models. Strong association in intermodel diversity between mode water and STCC offers additional support for the mode water's dynamic effect on STCC. Some models from CMIP5 include the Hawaii islands, the island-induced wind curls force the HLCC. The HLCC is located just to the south of the eastern STCC, consistent with the Sverdrup flow.

[34] We have also examined the STCC and mode water response to global warming by ensemble mean and intermodel difference among models. In global warming, all 17 CMIP5 models simulate the reduced mode water formation, consistent with CMIP3 results of *Luo et al.* [2009b]. The weakened mode water slows down STCC, consistent with GFDL CM2.1 results [*Xu et al.*, 2012]. The weakening of STCC and mode water is highly robust because the reduced mode water is due to the increase in upper ocean stratification, which itself is one of the most robust changes in global warming. The SSH anomalies in response to global warming exhibit a banded structure, similar to the negative phase of a decadal mode of STCC variability. In GFDL CM2.1 [*Xie*

et al., 2011] and CMIP5 (not shown), the northeast slanted bands of SSH in the central subtropical gyre represent a natural mode of STCC variability associated with changes in mode water ventilation. This natural mode of STCC variability is excited by global warming, resulting in banded structures in sea surface climate that correspond to a weakened STCC.

[35] RCP4.5 is a stabilization scenario where the total radiative forcing is stabilized around the late 2000s. Various components of the coupled ocean-atmosphere system respond to this external forcing at different time scales, including the fast response of the mixed layer and the slow response of the thermocline and deep water masses via ventilation and mixing. Formed in the surface mixed layer, mode water first shows a fast response to GHG forcing, and then a slow adjustment takes over (Figure 9b). We are investigating the full evolution of mode water response to global warming through 2300.

[36] **Acknowledgments.** This work is supported by the National Basic Research Program of China (2012CB955602), the China Scholarship Council, the U.S. National Science Foundation (0854365), the Natural Science Foundation of China (40830106, 40921004, and 41176006), and the Japan Agency for Marine-Earth Science and Technology. We thank the anonymous reviewers for constructive and helpful comments. We acknowledge the World Climate Research Programme's Working Group on Coupled Modeling, which is responsible for CMIP, and we thank the climate modeling groups (listed in Table 1 of this paper) for producing and making available their model output. This is IPRC/SOEST publication 931/8788.

References

Aoki, Y., T. Suga, and K. Hanawa (2002), Subsurface subtropical fronts of the North Pacific as inherent boundaries in the ventilated thermocline, *J. Phys. Oceanogr.*, *32*, 2299–2311, doi:10.1175/1520-0485(2002)032<2299:SSFOTN>2.0.CO;2.

Kobashi, F., and A. Kubokawa (2012), Review on North Pacific subtropical countercurrents and subtropical fronts: Role of mode waters in ocean circulation and climate, *J. Oceanogr.*, *68*, 21–43, doi:10.1007/s10872-011-0083-7.

Kobashi, F., H. Mitsudera, and S.-P. Xie (2006), Three subtropical fronts in the North Pacific: Observational evidence for mode water-induced subsurface frontogenesis, *J. Geophys. Res.*, *111*, C09033, doi:10.1029/2006JC003479.

Kobashi, F., S.-P. Xie, N. Iwasaka, and T. Sakamoto, (2008), Deep atmospheric response to the North Pacific oceanic subtropical front in spring, *J. Clim.*, *21*, 5960–5975, doi:10.1175/2008JCLI2311.1.

Kubokawa, A. (1997), A two-level model of subtropical gyre and subtropical countercurrent, *J. Oceanogr.*, *53*, 231–244.

Kubokawa, A. (1999), Ventilated thermocline strongly affected by a deep mixed layer: A theory for subtropical countercurrent, *J. Phys. Oceanogr.*, *29*, 1314–1333, doi:10.1175/1520-0485(1999)029<1314:VTSABA>2.0.CO;2.

Kubokawa, A., and T. Inui (1999), Subtropical countercurrent in an idealized ocean GCM, *J. Phys. Oceanogr.*, *29*, 1303–1313, doi:10.1175/1520-0485(1999)029<1303:SCIAIO>2.0.CO;2.

Luo, Y., L. M. Rothstein, and R.-H. Zhang (2009a), Response of Pacific subtropical-tropical thermocline water pathways and transport to global warming, *Geophys. Res. Lett.*, *36*, L04601, doi:10.1029/2008GL036705.

Luo, Y., Q. Liu, and L. M. Rothstein (2009b), Simulated response of North Pacific mode waters to global warming, *Geophys. Res. Lett.*, *36*, L23609, doi:10.1029/2009GL040906.

Nakamura, H. (1996), A pycnostad on the bottom of the ventilated portion in the central subtropical North Pacific: Its distribution and formation, *J. Oceanogr.*, *52*, 171–188, doi:10.1007/BF02235668.

Nonaka, M., S.-P. Xie, and H. Sasaki (2012), Interannual variations in low potential vorticity water and the subtropical countercurrent in an eddy-resolving OGCM, *J. Oceanogr.*, *68*, 139–150, doi:10.1007/s10872-011-0042-3.

Oka, E., and B. Qiu (2012), Progress of North Pacific mode water research in the past decade, *J. Oceanogr.*, *68*, 5–20, doi:10.1007/s10872-011-0032-5.

Qu, T., and J. Chen (2009), A North Pacific decadal variability in subduction rate, *Geophys. Res. Lett.*, *36*, L22602, doi:10.1029/2009GL040914.

Rio, M. H., S. Guinehut, and G. Larnicol (2011), New CNES-CLS09 global mean dynamic topography computed from the combination of GRACE data, altimetry, and in situ measurements, *J. Geophys. Res.*, *116*, C07018, doi:10.1029/2010JC006505.

Sakamoto, T. T., A. Sumi, S. Emori, T. Nishimura, H. Hasumi, T. Suzuki, and M. Kimoto (2004), Far-reaching effects of the Hawaiian Islands in the CCSR/NIES/FRCGC high-resolution climate model, *Geophys. Res. Lett.*, *31*, L17212, doi:10.1029/2004GL020907.

Suga, T., K. Hanawa, and Y. Toba (1989), Subtropical mode water in the 137°E section, *J. Phys. Oceanogr.*, *19*, 1605–1618, doi:10.1175/1520-0485(1989)019<1605:SMWITS>2.0.CO;2.

Suga, T., Y. Takei, and K. Hanawa (1997), Thermostad distribution in the North Pacific subtropical gyre: The central mode water and the subtropical mode water, *J. Phys. Oceanogr.*, *27*, 140–152, doi:10.1175/1520-0485(1997)027<0140:TDITNP>2.0.CO;2.

Suga, T., K. Motoki, Y. Aoki, and A. M. Macdonald (2004), The North Pacific climatology of winter mixed layer and mode waters, *J. Phys. Oceanogr.*, *34*, 3–22, doi:10.1175/1520-0485(2004)034<0003:TNPCOW>2.0.CO;2.

Taylor, K. E., R. J. Stouffer, and G. A. Meehl (2012), An overview of CMIP5 and the experiment design, *Bull. Am. Meteorol. Soc.*, *93*, 485–498, doi:10.1175/BAMS-D-11-00094.1.

Uda, M., and K. Hasunuma (1969), The eastward subtropical countercurrent in the western North Pacific Ocean, *J. Oceanogr. Soc. Jpn.*, *25*, 201–210.

White, W. B., K. Hasunuma, and H. Solomon (1978), Large-scale seasonal and secular variability of the subtropical front in the western North Pacific from 1954 to 1974, *J. Geophys. Res.*, *83*, 4531–4544, doi:10.1029/JC083iC09p04531.

Xie, S.-P., T. Kunitani, A. Kubokawa, M. Nonaka, and S. Hosoda (2000), Interdecadal thermocline variability in the North Pacific for 1958–1997: A GCM simulation, *J. Phys. Oceanogr.*, *30*, 2798–2813, doi:10.1175/1520-0485(2000)030<2798:ITVITN>2.0.CO;2.

Xie, S.-P., W. T. Liu, Q. Liu, and M. Nonaka (2001), Far-reaching effects of the Hawaiian Islands on the Pacific Ocean–atmosphere system, *Science*, *292*, 2057–2060, doi:10.1126/science.1059781.

Xie, S.-P., C. Deser, G. A. Vecchi, J. Ma, H. Teng, and A. T. Wittenberg (2010), Global warming pattern formation: Sea surface temperature and rainfall, *J. Clim.*, *23*, 966–986, doi:10.1175/2009JCLI3329.1.

Xie, S.-P., L. Xu, Q. Liu, and F. Kobashi (2011), Dynamical role of mode water ventilation in decadal variability in the central subtropical gyre of the North Pacific, *J. Clim.*, *24*, 1212–1225, doi:10.1175/2010JCLI3896.1.

Xie, S.-P., A. Kubokawa, F. Kobashi, and H. Mitsudera (2012), New developments in mode-water research: An introduction, *J. Oceanogr.*, *68*, 1–3, doi:10.1007/s10872-011-0090-8.

Xu, L. X., S.-P. Xie, Q. Liu, and F. Kobashi (2012), Response of the North Pacific Subtropical Countercurrent and its variability to global warming, *J. Oceanogr.*, *68*, 127–137, doi:10.1007/s10872-011-0031-6.

Yamanaka, G., H. Ishizaki, M. Hirabara, and I. Ishikawa (2008), Decadal variability of the Subtropical Front of the western North Pacific in an eddy-resolving ocean general circulation model, *J. Geophys. Res.*, *113*, C12027, doi:10.1029/2008JC005002.

Yoshida, K., and T. Kidokoro (1967), A subtropical countercurrent in the North Pacific—An eastward flow near the subtropical convergence, *J. Oceanogr.*, *23*, 88–91.